VolcAshDB open services for visualization and semi-automated classification of volcanic ash particles

Damià Benet*[1], Kévin Migadel[1], Fidel Costa[1]
[1] Institut de Physique du Globe de Paris, Paris, France
* dbenet@ipgp.fr [corresponding author]
ORCiD (FA): 0000-0002-5186-7048
ORCiD (SA): 0009-0006-0147-3354
ORCiD (TA): 0000-0002-1409-5325
Keywords: Volcanic ash; Database; Classification; Machine Learning; Web service; Open-source

THIS MANUSCRIPT HASN'T BEEN PEER-REVIEWED AND IS CURRENTLY UNDER REVIEW IN VOLCANICA.

Abstract

Volcanic ash particles contain critical pieces of information about their origin and the processes driving the eruptive activity. However, the classification of particles into different types (juvenile, lithic, free crystal, altered material) is not standardized and varies from observer to observer. As a result, datasets produced by different research groups are often difficult or not possible to compare, which limits the intercomparison and thus generalization between eruptive episodes within and between volcanoes. To address this, we developed the Volcanic Ash DataBase (VolcAshDB), an open repository of ash-particle data accessible through a web platform (volcashdb.ipgp.fr), and used it to build machine-learning classifiers for more objective and reproducible classification. Here, we present three new web services for particle visualization and semi-automatic classification. We show how users can browse and download different datasets of particles using advanced filters, generate visual summaries, and compare particle populations across volcanoes and eruptive styles. We also provide a service for semi-automatic ash particle classification that requires small prior user knowledge based on

a Vision Transformer (ViT) trained on the VolcAshDB dataset in January 2024. The service includes (i) optional image processing to help users process images before upload, (ii) a pre-classification check that evaluates whether uploaded images are similar to the training set using an Out-of-Distribution (OOD) method, and (iii) an automatic classification into the main particle types using probabilities. We evaluated the classifier on 600 new multi-focused binocular particle images from five volcanoes. The model yielded an average accuracy of 0.86. The pre-classification check adds a reliability layer by identifying uploads that fall outside the range covered by the training images, helping users interpret predictions. Together with the relatively good performance on new data, the classification service should be useful for componentry studies. As VolcAshDB grows to include additional samples and imaging setups, we expect performance to further improve, supporting a more robust and generalizable classifier for global comparisons of ash componentry and, ultimately, near real-time petrologic monitoring of volcanic eruptions.

Introduction

An ever-increasing amount of data in volcanological research plays a vital role in improving our ability to anticipate volcanic activity and reduce risk. For instance, the greater completeness of the eruptive records helps establishing magnitude-frequency relationships to model return periods aiding assessment of the risk (Condit & Connor, 1996; Deligne et al., 2010; Ho, 2008). Time-series monitoring of various data types are used to interpret pre- and syn-eruptive processes that may warn of a transition into a more explosive phase, e.g. scalation of seismicity prior to the 2010 Merapi, Indonesia (Jousset et al., 2013), inflation-deflation patterns preceding intensified explosive events in Sakurajima volcano, Japan (Ishii & Iguchi, 2024) or geochemical changes in precursory activity at Mt Taranaki, New Zealand (Green et al., 2013).

To obtain and be able to properly use such wealth of high-quality data, researchers often use procedures that are tailored to the specific volcanoes or eruptions at hand. This specificity allows to capture the subtle variations of a given event, but hinders the generality and integration of datasets across volcanoes or research teams, limiting the ability to derive global statistical insights (e.g., identification of volcano analogues; Tierz et al. 2019; Burgos et al. 2023). Therefore, there is a need for data interoperability that has become more pressing with advances in

data storage and the emergence of Machine Learning (ML) techniques capable of processing large datasets and extracting new insights (Carniel & Guzmán, 2025).

ML-driven research has been recently shown to be very fruitful for analysis of seismic data analysis from different volcanoes and eruptions (Ardid et al., 2025). At the same time, ML models may fail when applied beyond the conditions represented in their training data. This limitation has been documented in volcano-seismic monitoring: classifiers trained on a closed set of event types can confidently misclassify previously unseen signals. A common solution is to add an Out-of-Distribution (OOD) check to flag inputs that fall outside the training domain (Espinosa-Curilem et al., 2025) indicating when model outputs are likely to be reliable and when they should be interpreted with more caution.

The need for standardization and processing has motivated the development of shared infrastructure and services with the views of mitigation of volcano hazards (Trasatti et al., 2021). At the European level for instance, the Volcano Observations Thematic Core Service, part of the European Plate Observing System (EPOS), coordinates researchers and volcano observatories to implement a framework for providing access to multiple data, software and services (Puglisi et al., 2022; Spampinato et al., 2024). At the global level, WOVOdat hosts a database of volcanic unrest. It compiles a wide variety of data (seismic, deformation, hydrological, thermal, amongst others) in a standardized structure from approximately 1,500 different monitoring stations and provides users with services for data search and statistical tools (Costa et al., 2019; Nang et al., 2025; Newhall et al., 2017; Widiwijayanti et al., 2024).

In practice, many volcanological data types are still not standardized (Andrews et al., 2022; Trasatti et al., 2021), and this is the case in the classification of volcanic ash particles. Ash is made of particles from various origins that can be indicative of the processes driving the activity (e.g., Miwa et al. 2009; Andronico et al. 2021; Taddeucci et al. 2023). Petrologists have developed observational and analytical procedures to classify the particles into different types that have genetic implications (Alvarado et al., 2016; Benet et al., 2021; Gaunt et al., 2016; Miwa et al., 2009; Taddeucci et al., 2002). For instance, juvenile particles originate from magma near the surface whereas the lithic particles are fragments of older rock sources from the volcanic system. Despite its valuable

insights, the classification of particles into types (a task known as componentry analysis) has remained underutilized because classification is difficult, and criteria may vary depending on the volcano, eruption, and the observer (Alvarado et al., 2016; Pardo et al., 2014).

To alleviate this situation the Volcanic Ash DataBase (VolcAshDB) was developed (Benet, Costa, Widiwijayanti, et al., 2024; Benet et al., 2025) with the main aims of : (i) providing a quick and intuitive access to a large number of classified ash particle images from a range of eruptive styles and volcanoes (volcashdb.ipgp.fr); and (ii) using its contents to train ML models to classify ash particles in a reproducible and systematic manner. Here we present three new services that allow for visualization and classification of volcanic ash particles. These include (i) the *Catalogue*, which allows visualization and download of the dataset with advanced filters, (ii) the *Plots*, comprising summary plots of the contents and comparing data distributions between volcanoes, and (iii) the *Classify*, which allows users to classify their own images of particles including a pre-classification similarity check to flag images that fall outside the range covered by the training set. We show that preliminary results of the classifier with new, unseen data show decent performance and thus should be useful to complement expert, observer-based classification. All services, research products and software are free and open source.

Methods and materials

VolcAshDB structure

VolcAshDB is structured as a centralized repository of ash particles' data. It currently contains data from 11,808 particles and each particle is associated with a multi-focused binocular image, 33 physical characteristics related to the shape, texture and color, and a classification label that contains information about the type of particle (juvenile, lithic, altered material or free-crystal) and its metadata. The dataset as of April 2026 is available in FIGSHARE (https://figshare.com/collections/_/7644656) and its acquisition and coverage is described in Benet et al. (2025).

The database uses MongoDB, a NoSQL database, to organize data into flexible, schema-less *collections*. These *collections* store and manage various data types, including the *Volcanoes* and *Eruptions collections* (Figure 1)

which record basic information such as the vent location, eruption date, main rock compositions, and are sourced from Smithsonian's "Volcanoes of the World" database (Global Volcanism Program, 2025). The *Ash-Forming Events (AFEs) collection* records information about the ash-forming event such as the date and its volcanic context (e.g., eruptive style). The *Samples collection* contains information about sampling details such as the location and collection technique, and laboratory procedures such as cleaning and sieving. The *Particles collection* contains a unique identifier for each particle, the particle main type (juvenile, lithic, altered material or free-crystal) given by the user, an image, metadata such as the image acquisition conditions, and 33 measured *features* of the particles' shape, texture and color.

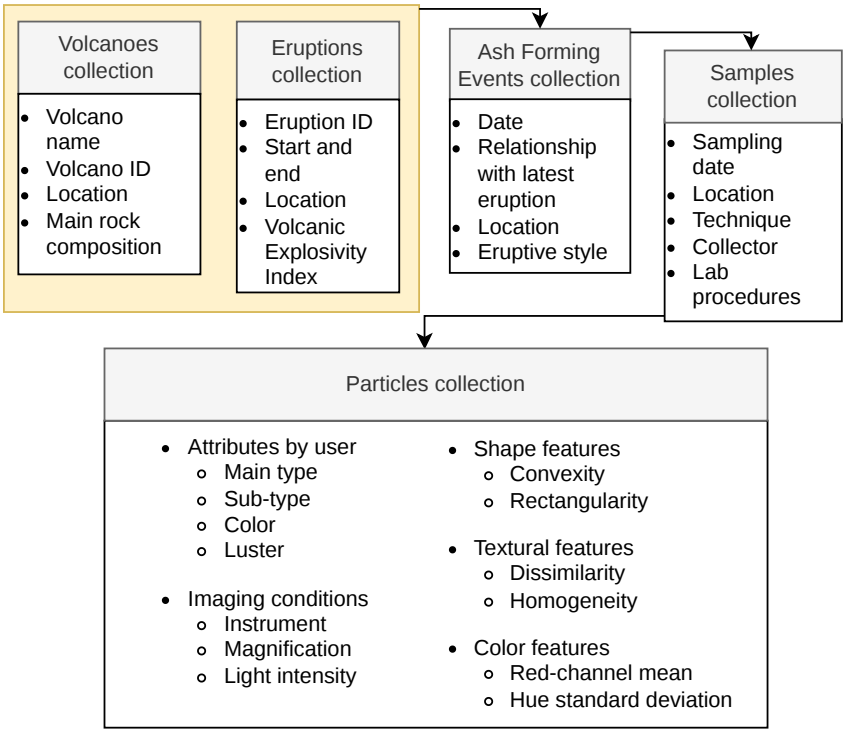

Figure 1: Schematic of the database hierarchical structure based on five MongoDB collections. Lists within bullet points are not exhaustive. Volcanoes and Eruptions collections in beige were adopted from Smithsonian's "Volcanoes of the World" database (Global Volcanism Program, 2025). The other collections are those in VolcAshDB.

VolcAshDB platform, web and services

Web-platform architecture and software

We developed a web-based platform to make the dataset and services open-access and easy to navigate. The platform is built using the MERN stack (MongoDB, Express.js, React.js, and Node.js) and runs on a virtual machine hosted by the Shared Virtualisation Service at the Institut de Physique du Globe de Paris (IPGP). It has two main components: (i) a backend that stores and manages the data, and (ii) a frontend that provides responsive interface for the services (Figure 2). The backend uses Node.js and Express.js for server-side functions, while MongoDB manages the data across the different *collections*. The frontend is developed in React.js and supports interactive exploration of the dataset and access to the classification service. Communication between the client and server is handled through a RESTful API. Below, we describe the three main services in VolcAshDB platform: *Catalogue*, *Plots* and *Classify.*

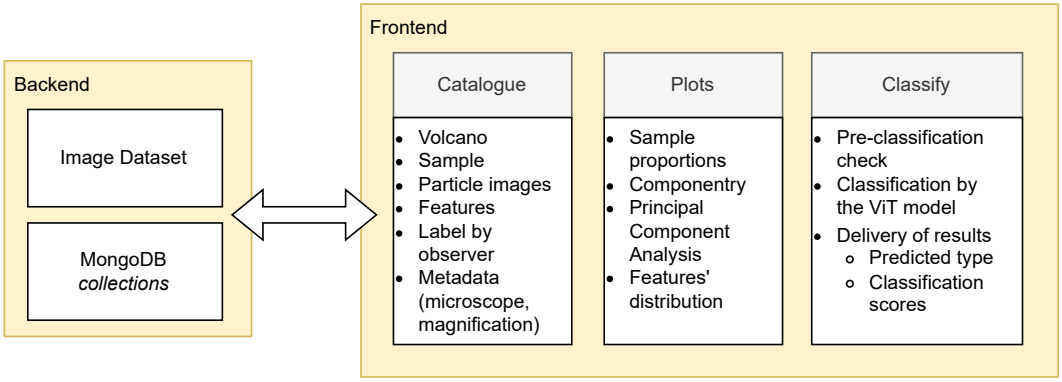

Figure 2: Dataflow and general architecture of VolcAshDB web-platform. The backend is the server-side part that users do not access directly; it handles data storage, authentication, and the requests sent by the frontend. The frontend is the user-facing part of the website (the pages and interactive elements displayed in the browser). Details of the MongoDB *collections* shown in Figure 1.

Catalogue service

The *Catalogue* (volcashdb.ipgp.fr/catalogue) allows users to effectively query, navigate and download the particle images in a user-friendly manner. For querying, we developed a system of tags with dropdown menus that allow filtering by volcano, eruptive activity type, grain-size fraction, particle type and shape (Figure 3). We added a search bar where users can type an element of interest to retrieve the images (e.g. the volcano name). All the metadata and features compiled for each particle can be accessed on screen by double-clicking the particle image.

Users can download the selected images and an excel spreadsheet with the particle features as a ZIP file after user verification. Verification is performed through an email confirmation step, where users receive an email with an activation link.

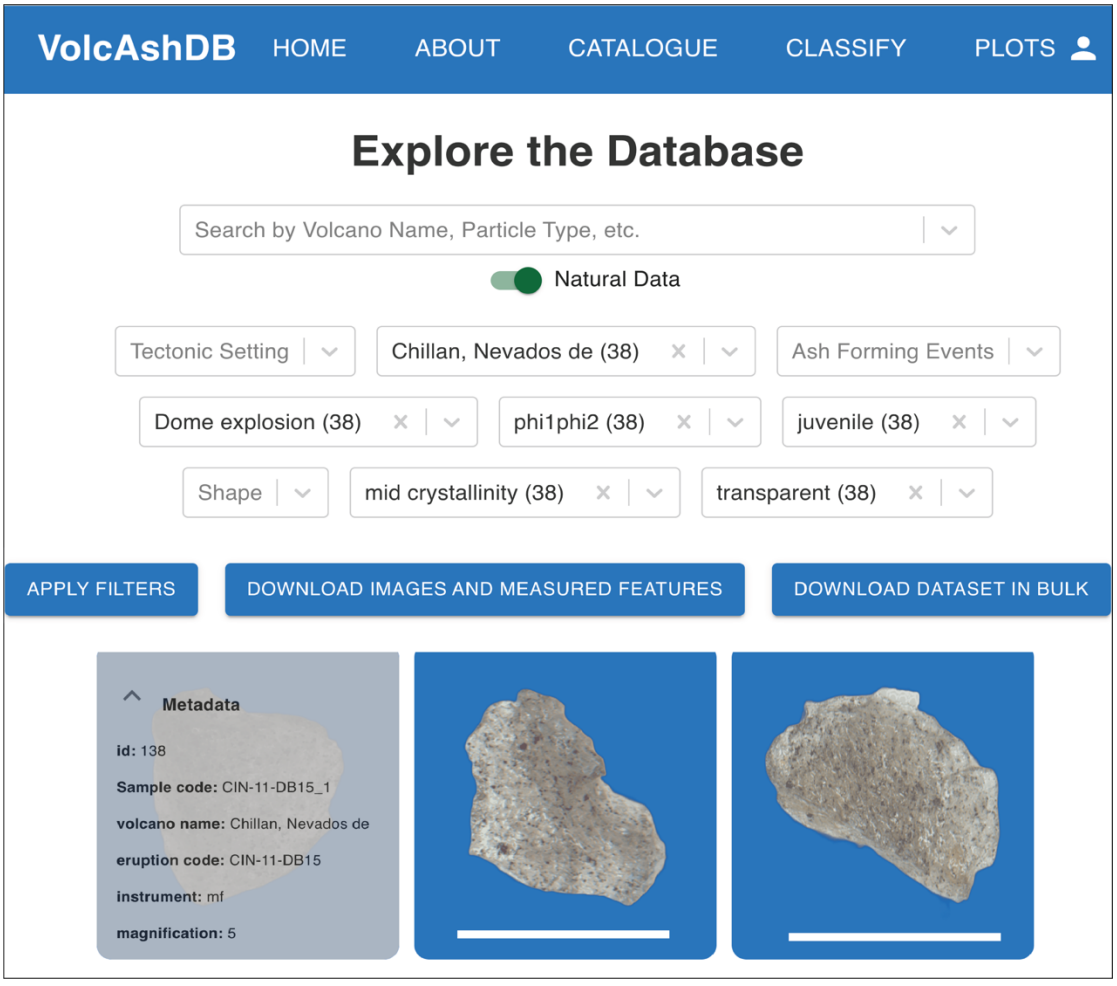

Figure 3: Screenshots of the *Catalogue* page in VolcAshDB web site. The white bars at the bottom of the particle images correspond to a 0.5 mm bar for scale.

Plots service

This service (volcashdb.ipgp.fr/analytic) provides visual summaries of the data which allows for user interaction. We divided the *Plots* into "Natural Data", for samples erupted by volcanoes, or "Experimental Data" for samples experimentally generated in the lab (see D'Oriano et al. 2013; Benet et al. 2025) (Figure 4). Pie charts show the

proportions of number of particles per volcano, per particle type, and per activity type. Ternary diagrams show the proportion of particle types normalized without free crystals per sample and according to eruptive activity type. We also use Principal Component Analysis of the features to display differences between different particle types (Benet et al. 2024a). Another available visualization is the histograms which show the distribution of values of a given feature and volcano. Further insights from all plots can be obtained by hovering with the mouse over any marker.

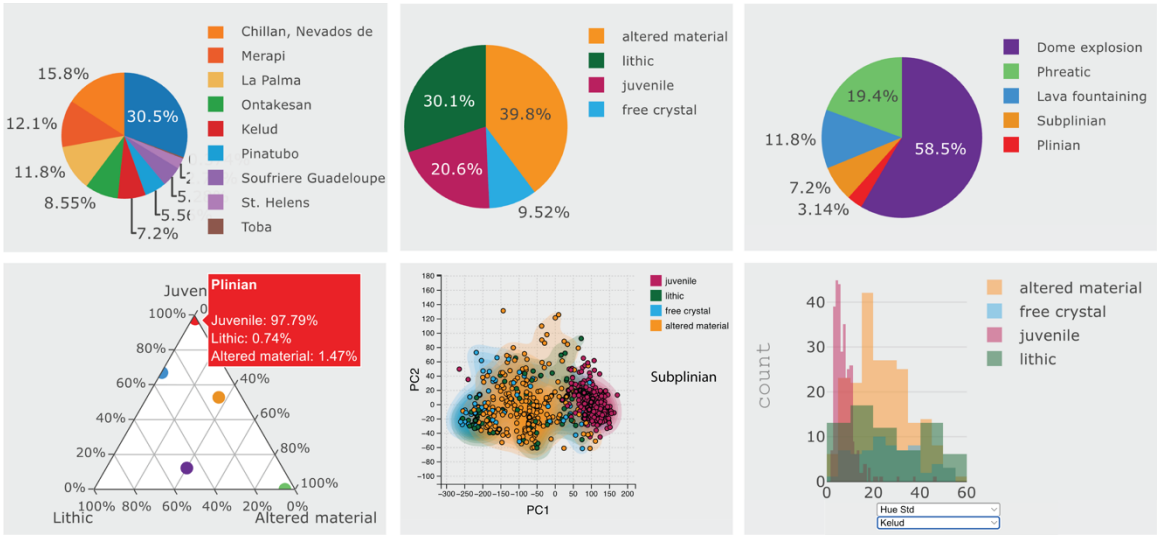

Figure 4: Screenshots of six representative panel plots from the *Plots* service page in VolcAshDB web site.

Classify service

The Classify service (volcashdb.ipgp.fr/classify) allows users to upload their own images of ash particles for particle classification and characterization. The underlying ash-particle classifier is a Vision Transformer (ViT) model trained on VolcAshDB image data as of January 2024. Details of model development are provided in Benet et al. (2024b). The service comprises three steps: (1) optional image processing to prepare user images for upload, (2) a pre-classification check that evaluates how similar the uploaded particle images are to the training images used to build the ViT, and (3) classification by the ViT, with results delivered to the user by email.

Step 1: Preparation of input image data

The classification service accepts images of individual ash particles. To maximize the model performance, we recommend a set of pre-processing tasks and provide an online tool in the interface of the *Classify* service. These procedures aim to reproduce the same image type that was used to train the ViT model.

First, we recommend acquiring images with a binocular microscope system that produces multi-focused images (i.e., images that are sharp across the full particle surface), such as the Leica LMT260 XY or the Keyence VHX-7000. If such systems are not available, multiple standard binocular images can be combined into a single multi-focused image using pre-trained deep learning models such as SESF-Fuse (Ma et al., 2021) or VAEEDOF (Piano et al., 2025).

Second, if an image contains multiple particles, it should be segmented into individual particle images prior to upload. This can be done in our *Classify* page by uploading the image (up to 2.5 GB) and cropping each particle by drawing bounding boxes in the interface (Figure 5A). Alternatively, automatic segmentation can be applied, for example using simple thresholding when particles have a clear contrast with the background (Wang, 2008) or using a deep learning segmentation model such as *Fast-SAM* (Zhao et al., 2023)

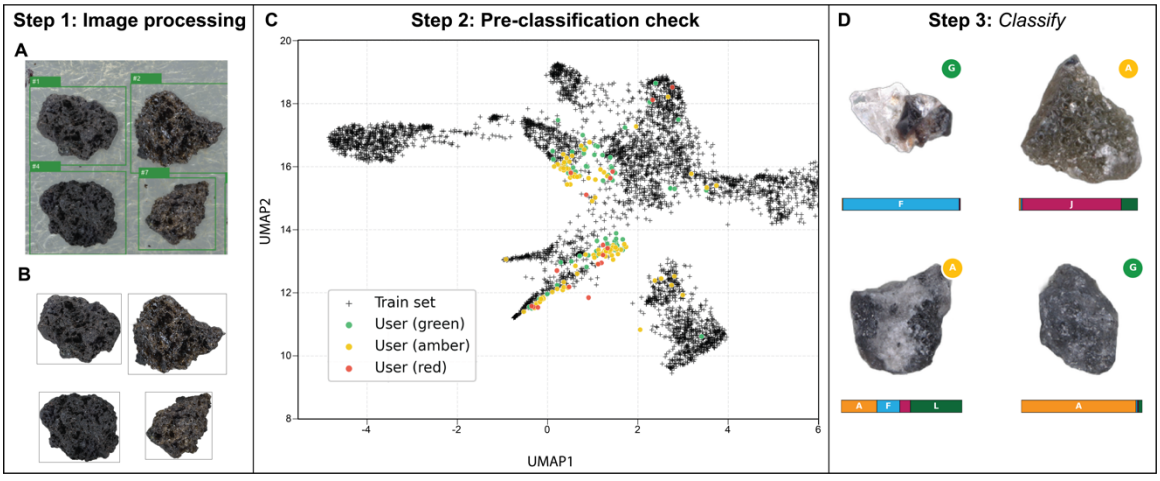

Figure 5: Workflow involved in the Classify service with screenshots of the outputted results. Image processing consists of (A) delineating bounding boxes and (B) image background removal. (C) UMAP representation of the ViT

embedding space used for the pre-classification check of the sample MAR-B. Uploaded images are plotted relative to the training-set distribution and colored by closeness: *Green* for images within the 5th–97th percentiles, *Amber* for those between the 97th and 99th percentiles, and *Red* for those beyond the 99th percentile. (D) The results from ash particle classification include the particle type and class-wise probabilities predicted by the model shown as horizontal stack bar where orange is for altered material (A), light blue for free-crystal (F), magenta for juvenile (J), and dark green for lithic (L). Note that each particle image, at the top-right corner, contains the given closeness color by the Out-of-Distribution analysis with a *G* for *Green*, *A* for *Amber* and *R* for *Red*.

Last, images should be provided with the background removed so that the classifier focuses on particle features rather than the imaging setup. This step is done automatically if using the tool from the *Classify* page (Figure 5B). Other alternatives for background removal include the built-in macOS workflow (right-click an image > Quick Actions > Remove Background), a free online service (https://www.rembg.com/en), or licensed software including Adobe Express Remove Background © or Adobe Photoshop © (Comida et al., 2022). Finally, the individual particle images should be placed in a single folder and compressed as a ZIP file prior to upload.

Step 2: Pre-classification check

Before running the ash classifier, we recommend to do a pre-classification check to assess whether the new ash-particle images to be classified are similar to those used to train the ViT. Users may upload either a small set of representative images (for example, covering the different particle types) or a larger batch, provided the total upload is <1 GB. This pre-classification check follows a standard Out-of-Distribution (OOD) approach (Kuan & Mueller, 2022), which we use here as a practical quality-control step. Each uploaded particle image is first processed by the ViT, and we compute the values produced at the penultimate layer, which summarize the image content just before the model assigns a class. We then compare these summaries with those from the training images to estimate how closely the upload matches the data used to build the classifier. These image summaries can also be visualized after dimensionality reduction (e.g. UMAP; McInnes et al. 2020), which helps inspect the embedding space and identify clusters of uploaded particles that fall outside the region occupied by the training set. Based on this comparison, a closeness colour is given according to where each uploaded image falls relative to the training reference range (Figure 5C): *Green* if the image lies within the central range of the training distribution (between the 0th and 97.7th percentiles), *Amber* if it lies near the edge of the training distribution (97.7th–99th percentiles), and *Red* if it falls beyond the 99th percentile. A high proportion of *Green* images indicates that the upload is well aligned with the training conditions and the predicted classes are expected to be more

reliable. In contrast, a high proportion of *Red* images suggests that the upload differs from the training images (due to image acquisition conditions, background or also particle characteristics), and the classification results should be treated with caution.

Step 3: Automatic model classification

After signing up and verification in the web platform, users can upload either a single image or a ZIP file containing multiple images (up to 1 GB). Once the upload is complete, processing starts automatically and, when finished, users receive an email containing a ZIP file with the outputs. The ZIP file includes: (i) a folder named "ood_analysis" with the results from Out-of-Distribution results including the closeness colors, a summary of the outputted values, and visualization of the results for each particle image; (ii) a folder named "results" with the ViT predictions "results.csv" file and a reference file containing all particles in the VolcAshDB dataset (volcashdb_particles.csv), structured in the same way as results.csv to facilitate comparisona; (iii) a folder named "visualizations" with a summary of the model predictions for each particle image, and a legend of the symbols and colors used; and (iv) a README file describing the content of each output file.

The "results.csv" file contains (i) the 33 particle features describing shape, texture, and color defined in Benet et al. (2024a), (ii) the particle type together with the class-wise probability predicted by the model (Benet, Costa, & Widiwijayanti, 2024), and (iii) the DOI of the publication describing the model (included because we plan to host multiple models in the future). The class-wise probabilities range from 0 to 1 and indicate how strongly the model supports each class or type of particle for a given image, with values closer to 1 corresponding to higher model confidence. These probabilities are intended as a practical indicator to help users interpret results, particularly for images flagged by the pre-classification check or cases where probabilities are similar across multiple classes, which may reflect ambiguity in particle classification (see Benet et al. 2024b for more details and explanation).

Evaluating ViT's performance with new samples and different image acquisition conditions

Data acquisition

To evaluate ViT's performance with new data (i.e. data that was not included in the training set of the model), we acquired particle data across various samples following the procedure in Benet et al. (2024a). For each particle, we obtained one multi-focused image and we classified it into one of the four main types (juvenile, lithic, altered material or free-crystal). We first cleaned the samples with several cycles of ultrasound baths of 15 s, dried overnight and sieved into grain-size fractions 0ϕ–1ϕ (i.e. between 2 to 1 mm of particle diameter), 1ϕ–2ϕ (1–0.5 mm) and 2ϕ–3ϕ (0.5–0.25 mm). Then, we laid the particles of the coarsest grain-size fraction to a transparent double-sticky tape glued on a glass slide and re-arranged the particles as a grid with the help of a needle. The glass slide was then scanned with a Keyence VHX-7000 optical microscope and software system at IPGP with a magnifying lens of x100 and light intensity value of 130. Particle images were segmented using the *FastSAM* model (Zhao et al., 2023), and we obtained an average resolution per image of about 750 x 750 pixels. The particle was classified based on diagnostic observations of particle features (Benet, Costa, Widiwijayanti, et al., 2024): Juvenile particles are generally glossy, smooth-surfaced, sharp-edged with a fresh aspect. Lithic particles are dark, dull, with subrounded edges. Altered material exhibits white, yellow or red coatings, can have a granular texture, and often exhibits signs of alteration such as dissolution surfaces. Free crystals can be recognised for their optical characteristics like the crystal habit, cleavage or twinning.

Sample descriptions

We evaluated ViT's performance using a range of samples, some included in the training set and others not (Table 1). By training set, we mean the image data from samples used in the model that learned the patterns for classification in Benet et al. (2024b). Here we used the following samples: (1) Ash particles from the Sub-plinian phase of February 2014 Kelud volcano (Indonesia) and the lava fountaining of Tajogaite eruption (Canary Islands), October 2021 that were included in the training set but which were imaged with a different microscope system; (2) samples from Nevados de Chillán volcano (Chile), January 2018, and La Soufrière de Guadeloupe (Antilles), August 1977, both of which are samples not covered in the training set, although the volcanoes and eruption were; and (3) Marapi (Indonesia), December 2023, which is a volcano not covered in the training set.

Model evaluation

The ViT's predictions were categorized into: True Positives (TP), where the prediction correctly matches the particle type given by the user, True Negative (TN), where the prediction correctly identifies the absence of a particle type; False Positive (FP), where the prediction wrongly identifies the presence of a particle type, and False Negatives (FN), where the prediction wrongly identifies the absence of a particle type. We evaluated the model's performance using the *macro F1-score* which is defined as the harmonic mean of precision and recall:

$$\text{F1-score} = 2 \cdot \frac{Precision\ x\ Recall}{Precision+Recall} \quad (1)$$

where $Precision = \frac{TP}{TP+FP}$ (2) and $Recall = \frac{TP}{TP+FN}$ (3)

We calculated the overall performance per sample using the *macro F1-score* which results from averaging the *F1-score* per each particle type, as opposed to the *weighted F1-score*, which also takes into account the number of particles that have been predicted per type. The *macro F1-score* is recommended for imbalanced datasets when FN and FP are equally important (Brownlee, 2020).

Simulating different image acquisition conditions

We acquired images and simulated gradual changes in a range of image conditions to assess the effect on ViT's performance. First, we increased the blur of the images to simulate a loss in image resolution. For this, we passed a Gaussian kernel from the *scikit-image* library at increasing values of blurring intensity which is measured in sigmas (σ). Second, we used the Gaussian kernel to incrementally blur most of the particle image while keeping a region in good focus as a proxy for single-focus images. Third, we varied the image brightness by using the *Pillow's* function *ImageEnhance.Brightness*, where an enhancement factor of 0 makes the image black, 1 is the original, and values above increases brightness. Lastly, we evaluated ViT's performance across varying thicknesses of the margin (i.e. the border between the particle and the image edges), measured in steps. Each step is defined as an integer (n) multiple of one-fifth of the particle diameter (D): step = $n \cdot D/6$. A set of 10 images for each parameter are shown in Fig. S1 in Supplementary Material 1.

Results and discussion

ViT's performance under varying imaging conditions

For this analysis we used the 600 new particle images and investigated the effect of low-resolution images of the entire particle or part of it, changes in brightness, and the thickness of the image margin (Figure 6). We also blurred our original particle images (average pixel resolution of ~ 750 x 750).

Effect of blur

We found that for blurring, the ViT performance peaks between 0–1 σ and remains at an overall performance > 0.9 *macro F1-score* until 4 σ (Figure 6A). For a Gaussian blur > 4 σ, the accuracy decreases at a higher rate, particularly the lithic particle type reaching a *F1-score* of 0.75 at 10 σ. Considering that our images at 4 σ yield lower but relatively good accuracy, we recommend the use of images with a resolution of at least 500 x 500 pixels.

Effect of single versus multi-focused images

To evaluate the effect of using single-focus images, we increasingly blurred the original images using the Gaussian blur as above but leaving a part of it in good focus (Figure 6B). The starting blur is at 10 σ yielding 0.91 of *macro F1-score*. This suggests that the model is able to identify discriminant information from single-focus-like images with resolution ~750 x 750 pixels. Increasing blur between 10–50 σ yields a progressive drop of *F1-score* by more than 0.1. The free crystals are particularly misclassified likely because their planar surfaces and bright reflections, which are discriminant, were partially erased when blurring. It is worthy to note that the classification of juvenile particles remains quite accurate (> 0.90 *F1-score*).

Effect of rescaling pixel intensity

We also investigated the effect of rescaling the image pixel values to lower (darker) or higher (brighter) values using a brightness factor. Our images were acquired at a light intensity of 130 in the Keyence VHX-7000, which is represented as a brightness factor of 1 in these simulations (Figure 6C). The ViT yields relatively high accuracy

above 0.90 *macro F1-score* within a narrow range of ± 0.1. When the variation in brightness factor is higher than ± 0.2, the *F1-score* drops significantly by more than 0.1 at 0.6 (dark) and 1.3 (bright) of brightness factor. This suggests that the ViT can handle well some variations in light intensity.

315

Effect of particle's margin thickness

We evaluated how margin thickness affects ViT performance. The margin is the image border between the particle contour and the image boundaries. We parameterized the margin thicknesses in steps, where each step is an integer (n) multiple of one-sixth of the particle diameter (D) (step = $n \cdot D/6$). With margin = 0, ViT performs
320 best (*macro F1-score* = 0.94). At a margin of 1 step, the macro F1-score drops abruptly by up to 0.3. For margins >1 step, performance gradually recovers toward its original accuracy. This indicates that the model is sensitive to the spatial context introduced by the margin, and we recommend removing it by cropping the image.

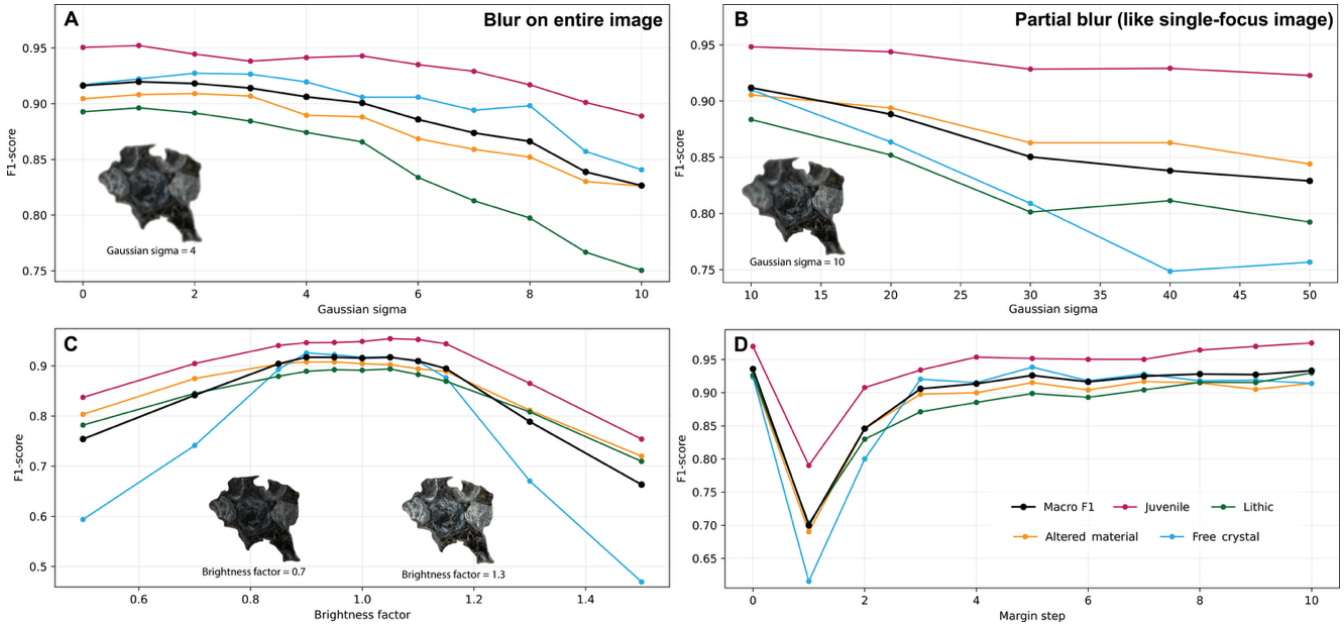

Figure 6: Plots with modelled *F1-scores* showing the effect of image variations: (A) Gaussian blur applied to the entire
325 **image (proxy for reduced resolution), (B) partial Gaussian blur (proxy for single-focus imaging), (C) brightness scaling, and (D) image-margin thickness (expressed in steps).**

Testing the pre-classification check with new samples

We applied the pre-classification Out-of-Distribution (OOD) check to the 600 particles from five different samples with variable overlap with the ViT training set (see section "Samples" and Table 1 for details) to evaluate how closely these new images match the training set. In addition, we analysed a subset of 100 particles from the ViT test set (Benet, Costa, & Widiwijayanti, 2024) which shares the same samples and imaging conditions as the training data, and used it as a reference where most particles are expected to fall within the training distribution. We found that 97% of the test-set particles were flagged as *Green* (between the 5^{th} and 97^{th} percentiles of the training set distribution), with only 3% flagged as *Amber* (Table 2).

The new samples show a higher proportion of *Amber* (42–65%), and to a lesser extent *Red* particles (19–56%; Table 2) consistent with the fact that one or more key factors (volcano, sample, and/or microscope) are not represented in the training set (Table 1). In particular, SG-DB3 is almost entirely *Red* and *Amber* with 56% and 42% respectively. Visualization of the SG-DB3 distribution shows that it forms a cluster out of the training distribution through the UMAP (Figure 7). However, as shown below, all SG-DB3 particles are correctly classified by the model as altered material, indicating that the pre-classification check captures difference from the training domain rather than expected failure of the classifier. By contrast, particles from B-MAR are mostly classified as *Green* (31%) and *Amber* (50%), while the remaining 19% are flagged as *Red*. As shown below, this *Red* fraction includes a group of particles that is systematically misclassified, suggesting that in this case the pre-classification check successfully highlights the part of the dataset that is least represented in the training set and most prone to error.

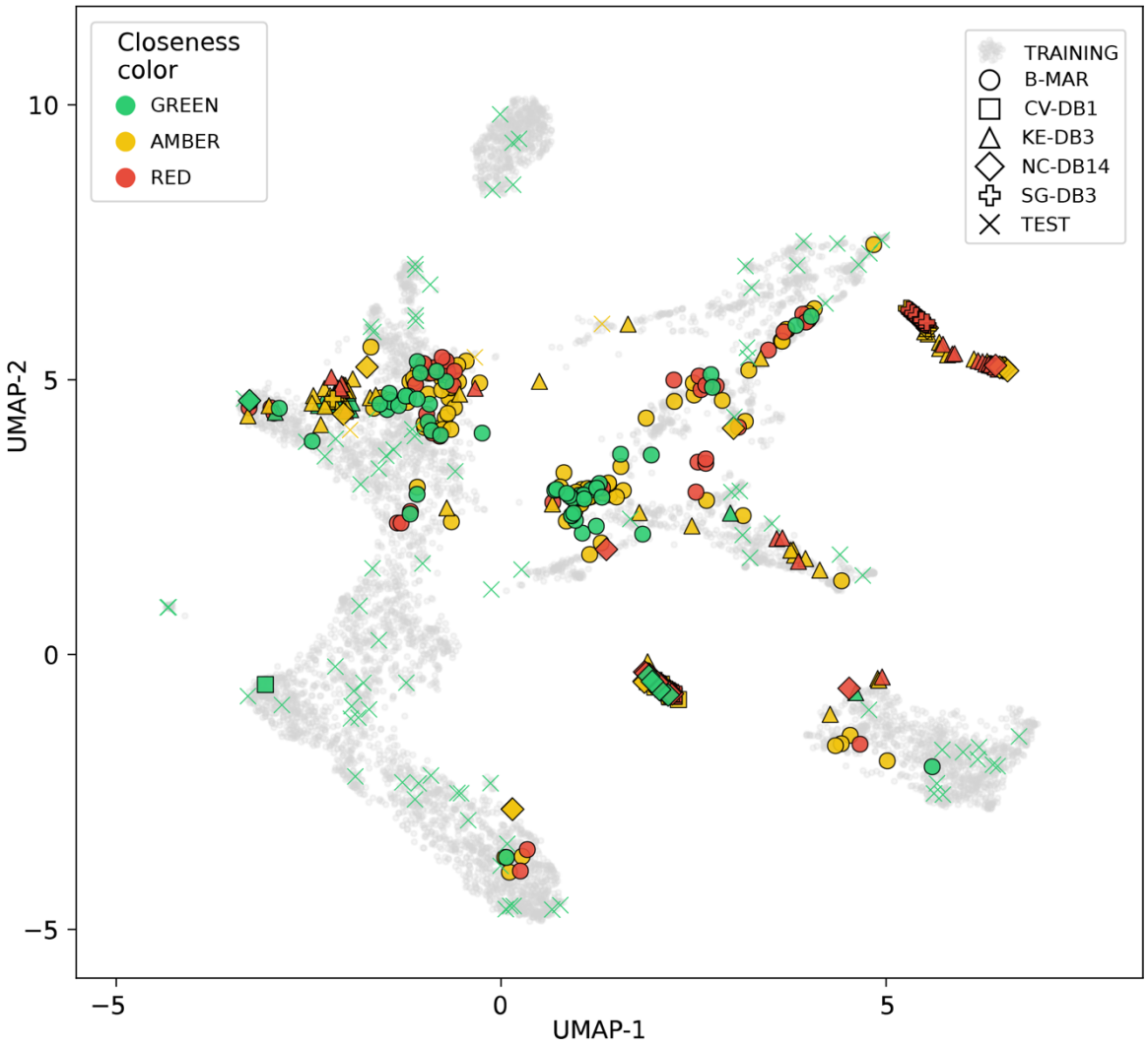

Figure 7: UMAP projection of the ViT embedding space used for the pre-classification check. Grey dots represent the training images, whereas symbols correspond to particles from the reference test set and the five new samples. Each particle is colored according to its closeness to the training distribution: *Green* if it falls within the 5th–97th percentile range, *Amber* between the 97th and 99th percentiles, and *Red* beyond the 99th percentile. The plot allows visual inspection of how new datasets overlap with, or diverge from, the training-set distribution, including the presence of clusters that lie partly or entirely outside the main training domain.

Testing ViT performance with new samples

The results of the model of the five new samples yield a *macro F1-score* of 0.86 (Table 3) with juvenile particles being the most accurately classified (*macro F1-score* 0.89) and lithics the least accurate (*macro F1-score* 0.76).

Despite the high proportion of images flagged as *Red* in several samples, classification performance remains generally robust, but errors occur more frequently for particles that deviate most from the training domain.

The particles from KE-DB3 are from the same sample and volcano as those included in the training set, but they were imaged with a different microscope setup. The *macro F1-score* is 0.85 (Table 3), lower than the original test-set performance (*macro F1-score* of 0.91; Benet et al. 2024b) indicating that the use of a different microscope and image software can affect performance even if both sets of images are multi-focused and acquired following the same procedure. For example, there is a cluster of juvenile particles that are predicted by the ViT as altered material (Figure 8A). While the juvenile, true positives have a well-defined vesicularity (Figure 8I), the false positives have vesicles partially blur (Figure 8II).

The particles from Cumbre Vieja (CV-DB1) volcano also come from the same sample as the training set, but were also imaged with a different microscope setup. The *macro F1-score* is 0.83, lower than the 0.91 reported for the original test set (Benet, Costa, & Widiwijayanti, 2024). The sample consists of two particle types, i.e. lithics (mostly recycled juveniles) and juvenile particles (Figure 8B). The model generally classifies well dull particles with signs of recrystallization (Figure 8III) but can misclassify as juvenile particles with metallic reflexions (Figure 8IV) typical of recycling (D'Oriano et al., 2014). This could be due to the different interaction of the reflections with the light condenser of the Keyence VHX-7000 microscope and how the software handles them respect to the original imaging setup.

Samples from Nevados de Chillán volcano were included in the training set, but here we analyzed a sample (NC-DB14) from a different erupted date although from the same eruptive cycle. The *macro F1-score* is 0.81, slightly lower than 0.85 reported for the original test set, suggesting that the model generalizes reasonably well to new material from the same eruptive cycle. We did not find a systematic misclassification of a cluster of particles, and it can be difficult to decide whether a mismatch in particle types between the ViT and the observer are classification mistakes by the model or the other way around. For instance, the ViT model classify as juvenile vesicular, glossy particles (Figure 8V) as well as those with adhered orange material on the surface (Figure 8VI). The latter was classified as altered material by the observer because its coatings were interpreted to originate

from interaction with the hydrothermal system. However, these coatings could also result from sublimation in the volcanic plume, maintaining its juvenile origin (Spadaro et al., 2002), which makes the distinction ambiguous.

Almost 100 particles from a new sample from La Soufrière de Guadeloupe (SG-DB3) volcano were correctly classified as altered material (Figure 8D). The particles are completely (Figure VII) or partially (Figure VIII) covered by white to yellow coatings and the model yields probabilities > 0.95 of belonging to altered material. The correct classification of these particles, which appears relatively straightforward, adds value to the capabilities of the model, especially in the context of the eruption of La Soufrière de Guadeloupe 1975–1977, where erratic classification of ash particles led to disputed interpretations of the processes driving the activity (Feuillard et al., 1983).

Finally, we also acquired data from 259 particles from the December 2023 Marapi volcano eruption, which was not included in the training set of the ViT. Classification by the model of these particles is relatively accurate with a *macro F1-score* of 0.81 (Figure 8D). The ViT correctly identifies most of the glossy, vesicular juvenile particles (Fig. 5IX), but almost 20% are misclassified as free crystals. Examination of the particle images reveals that some of these false positives consist of glassy, transparent particles with bright reflections, and the model assigns them to the free-crystal type with high confidence (e.g., probability of free-crystal = 0.99; Figure 8X). A likely explanation is that juvenile particles with the combined transparency and reflections were not included in the training set, and that the model associates them with plagioclase crystals, which were present in the training set.

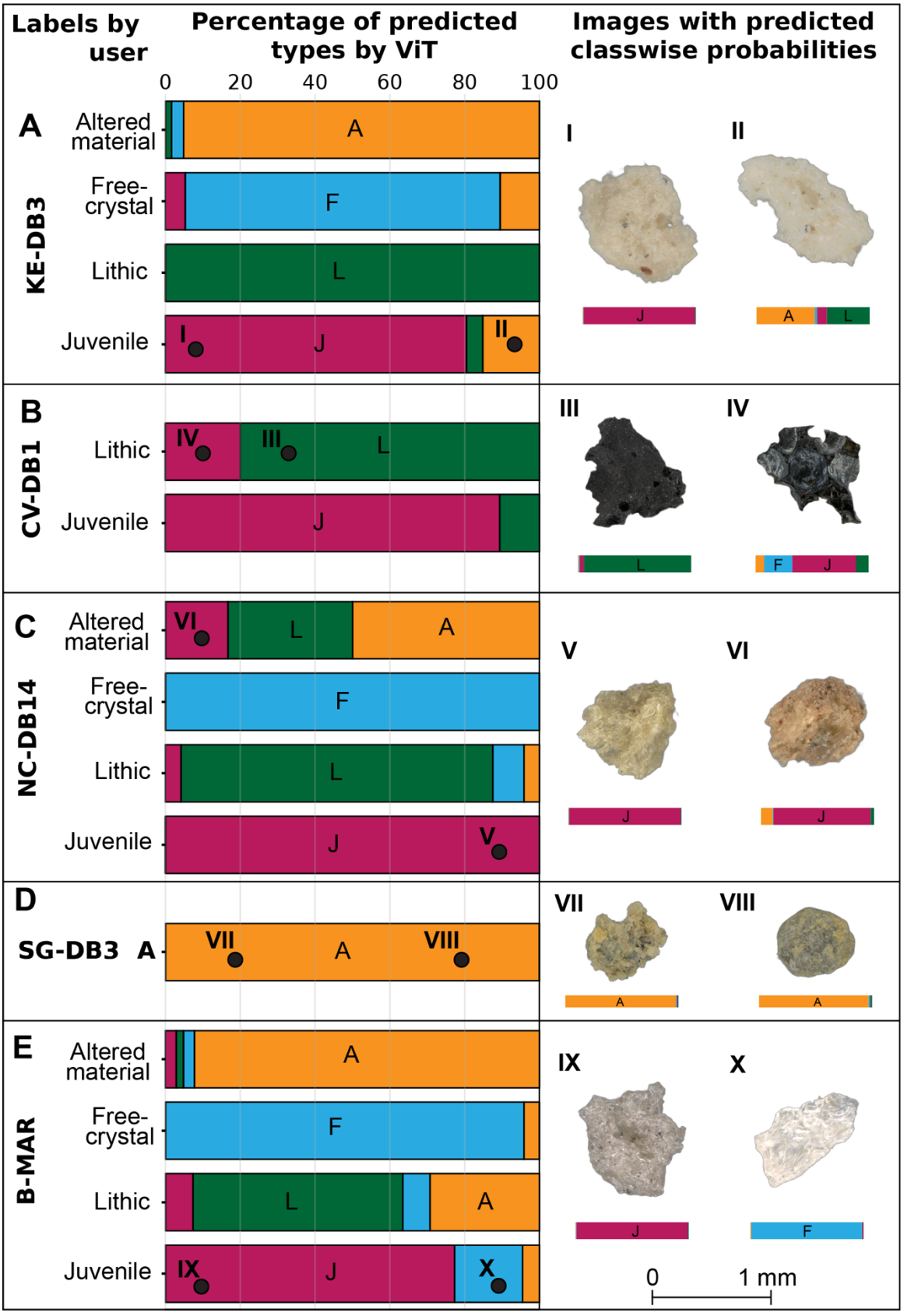
Labels by user
Percentage of predicted types by ViT
Images with predicted classwise probabilities
0
20
40
60
80
100
A
Altered material
Free-crystal
Lithic
Juvenile
KE-DB3
I
II
B
CV-DB1
III
IV
C
NC-DB14
VI
V
D
SG-DB3
VII
VIII
E
B-MAR
IX
X
0
1 mm

20

405

Figure 8: Bar charts showing the percentage of predicted types respect to the assigned label. If all predictions were of the same type as the observed, each bar would be single-colored as follows: orange for altered material (A), light blue for free-crystal (F), magenta for juvenile (J), and dark green for lithic (L). For each sample (A, B, C, D and E) we show two representative images. The particle type where each image belongs is mapped with a dot and associated with Roman numerals from I to X. Below each representative image, the horizontal bar shows the class-wise probabilities outputted by the model, using the same color scheme as the bar charts.

ViT's applicability and suggestions for comparison studies and petrologic monitoring

The web-based classification service we developed can be readily used to classify ash particles images into altered material, free-crystal, juvenile or lithic types. Our ViT provides a classification score that can support componentry analysis for understanding the processes that lead to the eruption as well as distinguishing phreatic, phreatomagmatic or magmatic events (Alvarado et al., 2016; Cioni et al., 1992; Heiken, 1974; Heiken & Wohletz, 1985; Pardo et al., 2014), the role of ash transport at different distances of the crater in impacting the componentry (Eychenne et al., 2013), and where detailed time-series of ash samples are available, to combine it with other observables for monitoring (Benet et al., 2021; Gaunt et al., 2016; Liu et al., 2020; Martin-Del Pozzo & Nieto-Torres, 2024). The classifier can generalize relatively well to new samples (Table 3). However, the ViT can systematically misclassify particles with distinctive, previously unseen features, such as transparent glass shards from Marapi (Figure 5E). We provide the pre-classification check for users to quantify the proportion of such "unseen" particles and get an intuition of the model's reliability. For optimal performance, we recommend using multi-focused images or, if unavailable, the highest possible resolution (> 500 x 500 per particle image), and we provide a tool for cropping images and remove background.

Conclusions and future work

The ViT training dataset was acquired using a standardized imaging protocol designed to capture subtle variations in particle shape, texture, and color across particle types. This controlled approach produced a consistent dataset that helps reveal how particle-type distributions vary across eruptive styles. However, the same level of standardization also limits generalizability, because the model sees a narrow range of microscope setups and acquisition conditions during training. Improving generalizability therefore requires expanding the dataset to include images acquired with different microscopes, settings, and preparation conditions, and then retraining a

more robust classifier. VolcAshDB already hosts the current dataset, and the services presented in this work provide a practical entry point for adding new data and benchmarking performance. Ultimately, a systematic and reproducible particle classification will support consistent componentry, which is critical for volcano monitoring, and will allow for global-scale comparisons to identify broader relationships and similarities across datasets.

Author contributions

Damià Benet led the development, acquired and processed the data, and wrote the original manuscript of the project, which was supervised and revised by Fidel Costa. Kévin Migadel and Damià Benet led the development of front-end and the back-end of the new web-platform services. The final version of the manuscript has been read, reviewed and approved by all co-authors.

Acknowledgements

Damià Benet is very grateful to Pascale Besson for providing the sample from La Soufrière de Guadeloupe and to David Weissenbach and Michel Le Cocq from the Shared Virtualisation Service at IPGP for their help in setting up the virtual machine that runs VolcAshDB platform. Numerical computations were partly performed on the S-CAPAD/DANTE platform, IPGP, France. This research was supported by Fidel Costa's Chaire d'Excellence grant by the Université Paris Cité.

Data availability

Ash-particle data of both images and features is available through our *Catalogue* service (volcashdb.ipgp.fr/catalogue) and as an open repository in FIGSHARE (https://figshare.com/collections/_/7644656). The source code of VolcAshDB web-platform is available in the GitHub repository: https://github.com/dbenet-ntu/VolcAshDB-web_Apr2026.

References

Alvarado, G. E., Mele, D., Dellino, P., de Moor, J. M., & Avard, G. (2016). Are the ashes from the latest eruptions (2010–2016) at Turrialba volcano (Costa Rica) related to phreatic or phreatomagmatic events? *Journal of Volcanology and Geothermal Research*, *327*, 407–415. https://doi.org/10.1016/j.jvolgeores.2016.09.003

Andrews, B. J., Costa, F., Venzke, E., & Widiwijayanti, C. (2022). Databases in Volcanology. *Bulletin of Volcanology*, *84*(10), 92. https://doi.org/10.1007/s00445-022-01597-x

Andronico, D., Del Bello, E., D'Oriano, C., Landi, P., Pardini, F., Scarlato, P., de' Michieli Vitturi, M., Taddeucci, J., Cristaldi, A., Ciancitto, F., Pennacchia, F., Ricci, T., & Valentini, F. (2021). Uncovering the eruptive patterns of the 2019 double paroxysm eruption crisis of Stromboli volcano. *Nature Communications*, *12*(1), 4213. https://doi.org/10.1038/s41467-021-24420-1

Ardid, A., Dempsey, D., Caudron, C., Cronin, S., Kennedy, B., Girona, T., Roman, D., Miller, C., Potter, S., Lamb, O. D., Martanto, A., Cubuk-Sabuncu, Y., Cabrera, L., Ruiz, S., Contreras, R., Pacheco, J., Mora, M. M., & De Angelis, S. (2025). Ergodic seismic precursors and transfer learning for short term eruption forecasting at data scarce volcanoes. *Nature Communications*, *16*(1), 1758. https://doi.org/10.1038/s41467-025-56689-x

Benet, D., Costa, F., Migadel, K., Lee, D. W. J., D'Oriano, C., Pompilio, M., Nurfiani, D., & Rifai, H. (2025). A repository-hosted dataset of volcanic ash particle images and features. *Scientific Data*, *12*(1), 681. https://doi.org/10.1038/s41597-025-04942-9

Benet, D., Costa, F., Pedreros, G., & Cardona, C. (2021). The volcanic ash record of shallow magma intrusion and dome emplacement at Nevados de Chillán Volcanic complex, Chile. *Journal of Volcanology and Geothermal Research*, *417*, 107308. https://doi.org/10.1016/j.jvolgeores.2021.107308

Benet, D., Costa, F., & Widiwijayanti, C. (2024). Volcanic Ash Classification Through Machine Learning. *Geochemistry, Geophysics, Geosystems*, *25*(3), e2023GC011224. https://doi.org/10.1029/2023GC011224

Benet, D., Costa, F., Widiwijayanti, C., Pallister, J., Pedreros, G., Allard, P., Humaida, H., Aoki, Y., & Maeno, F. (2024). VolcAshDB: A Volcanic Ash DataBase of classified particle images and features. *Bulletin of Volcanology*, *86*(1), 9. https://doi.org/10.1007/s00445-023-01695-4

Brownlee, J. (2020). *Imbalanced Classification with Python: Choose Better Metrics, Balance Skewed Classes, and Apply Cost-Sensitive Learning* (v1.2).

Burgos, V., Jenkins, S. F., Bono Troncoso, L., Perales Moya, C. V., Bebbington, M., Newhall, C., Amigo, A., Prada Alonso, J., & Taisne, B. (2023). Identifying analogues for data-limited volcanoes using hierarchical clustering and expert knowledge: A case study of Melimoyu (Chile). *Frontiers in Earth Science*, *11*. https://doi.org/10.3389/feart.2023.1144386

Carniel, R., & Guzmán, S. R. (2025). Machine Learning for Volcanology and Volcano Monitoring. In Z. Spica & C. Caudron (Eds.), *Modern Volcano Monitoring* (pp. 421–459). Springer Nature Switzerland. https://doi.org/10.1007/978-3-031-86841-2_14

Cioni, R., Sbrana, A., & Vecci, R. (1992). Morphologic features of juvenile pyroclasts from magmatic and phreatomagmatic deposits of Vesuvius. *Journal of Volcanology and Geothermal Research*, *51*(1–2), 61–78. https://doi.org/10.1016/0377-0273(92)90060-Q

Comida, P. P., Ross, P.-S., Dürig, T., White, J. D. L., & Lefebvre, N. (2022). Standardized analysis of juvenile pyroclasts in comparative studies of primary magma fragmentation: 2. Choice of size fraction and method optimization for particle cross-sections. *Bulletin of Volcanology*, *84*(1), 14. https://doi.org/10.1007/s00445-021-01517-5

Condit, C. D., & Connor, C. B. (1996). Recurrence rates of volcanism in basaltic volcanic fields: An example from the Springerville volcanic field, Arizona. *GSA Bulletin*, *108*(10), 1225–1241. https://doi.org/10.1130/0016-7606(1996)108%253C1225:RROVIB%253E2.3.CO;2

Costa, F., Widiwijayanti, C., Nang, T. Z. W., Fajiculay, E., Espinosa-Ortega, T., & Newhall, C. (2019). WOVOdat – the global volcano unrest database aimed at improving eruption forecasts. *Disaster Prevention and Management*, *28*(6), 738–751. https://doi.org/10.1108/DPM-09-2019-0301

Deligne, N. I., Coles, S. G., & Sparks, R. S. J. (2010). Recurrence rates of large explosive volcanic eruptions. *Journal of Geophysical Research: Solid Earth*, *115*(B6). https://doi.org/10.1029/2009JB006554

D'Oriano, C., Bertagnini, A., Cioni, R., & Pompilio, M. (2014). Identifying recycled ash in basaltic eruptions. *Scientific Reports*, *4*(1), 5851. https://doi.org/10.1038/srep05851

D'Oriano, C., Pompilio, M., Bertagnini, A., Cioni, R., & Pichavant, M. (2013). Effects of experimental reheating of natural basaltic ash at different temperatures and redox conditions. *Contributions to Mineralogy and Petrology*, *165*(5), 863–883. https://doi.org/10.1007/s00410-012-0839-0

Espinosa-Curilem, C., Basualto, D., Curilem, M., & Huenupan, F. (2025). Volcano Seismic Event Recognition and OOD Detection using Multi-Representation Deep Learning: Insights from Nevados del Chillán. *Journal of Volcanology and Geothermal Research*, *466*, 108406. https://doi.org/10.1016/j.jvolgeores.2025.108406

Eychenne, J., Le Pennec, J. L., Ramón, P., & Yepes, H. (2013). Dynamics of explosive paroxysms at open-vent andesitic systems: High-resolution mass distribution analyses of the 2006 Tungurahua fall deposit (Ecuador). *Earth and Planetary Science Letters*, *361*, 342–355. https://doi.org/10.1016/j.epsl.2012.11.002

Feuillard, M., Allegre, C. J., Brandeis, G., Gaulon, R., Le Mouel, J. L., Mercier, J. C., Pozzi, J. P., & Semet, M. P. (1983). The 1975–1977 crisis of la Soufriere de Guadeloupe (F.W.I): A still-born magmatic eruption.

Journal of Volcanology and Geothermal Research, *16*(3–4), 317–334. https://doi.org/10.1016/0377-0273(83)90036-7

Gaunt, H. E., Bernard, B., Hidalgo, S., Proaño, A., Wright, H., Mothes, P., Criollo, E., & Kueppers, U. (2016). Juvenile magma recognition and eruptive dynamics inferred from the analysis of ash time series: The 2015 reawakening of Cotopaxi volcano. *Journal of Volcanology and Geothermal Research*, *328*, 134–146.

Global Volcanism Program. (2025). *Volcanoes of the World* (Version v. 5.3.1) [Dataset]. compiled by E. Venzke. https://doi.org/10.5479/si.GVP.VOTW5-2025.5.3

Green, R. M., Bebbington, M. S., Cronin, S. J., & Jones, G. (2013). Geochemical precursors for eruption repose length. *Geophysical Journal International*, *193*(2), 855–873. https://doi.org/10.1093/gji/ggt044

Heiken, G. (1974). *Atlas of volcanic ash*. Smithsonian Contributions to the Earth Sciences.

Heiken, G., & Wohletz, K. (1985). *Volcanic Ash*. University Presses of California, Chicago, Harvard & MIT.

Ho, C.-H. (2008). Empirical recurrence rate time series for volcanism: Application to Avachinsky volcano, Russia. *Journal of Volcanology and Geothermal Research*, *173*(1), 15–25. https://doi.org/10.1016/j.jvolgeores.2007.12.003

Ishii, K., & Iguchi, M. (2024). Statistical analysis of the ground deformation of Vulcanian explosions at Sakurajima volcano, Japan. *Journal of Volcanology and Geothermal Research*, *455*, 108185. https://doi.org/10.1016/j.jvolgeores.2024.108185

Jousset, P., Budi-Santoso, A., Jolly, A. D., Boichu, M., Surono, Dwiyono, S., Sumarti, S., Hidayati, S., & Thierry, P. (2013). Signs of magma ascent in LP and VLP seismic events and link to degassing: An example from the 2010 explosive eruption at Merapi volcano, Indonesia. *Journal of Volcanology and Geothermal Research, Merapi Eruption*, *261*, 171–192. https://doi.org/10.1016/j.jvolgeores.2013.03.014

Kuan, J., & Mueller, J. (2022). *Back to the Basics: Revisiting Out-of-Distribution Detection Baselines* (arXiv:2207.03061). arXiv. https://doi.org/10.48550/arXiv.2207.03061

Liu, E. J., Cashman, K. V., Miller, E., Moore, H., Edmonds, M., Kunz, B. E., Jenner, F., & Chigna, G. (2020). Petrologic monitoring at Volcán de Fuego, Guatemala. *Journal of Volcanology and Geothermal Research*, *405*, 107044.

Ma, B., Zhu, Y., Yin, X., Ban, X., Huang, H., & Mukeshimana, M. (2021). SESF-Fuse: An unsupervised deep model for multi-focus image fusion. *Neural Computing and Applications*, *33*(11), 5793–5804. https://doi.org/10.1007/s00521-020-05358-9

Martin-Del Pozzo, A. L., & Nieto-Torres, A. (2024). Ashfall characteristics and development of the ash monitoring network during three decades of the long-lived eruption of Popocatépetl Volcano, México. *Journal of Volcanology and Geothermal Research*, *454*, 108176. https://doi.org/10.1016/j.jvolgeores.2024.108176

McInnes, L., Healy, J., & Melville, J. (2020). *UMAP: Uniform Manifold Approximation and Projection for Dimension Reduction* (arXiv:1802.03426). arXiv. https://doi.org/10.48550/arXiv.1802.03426

Miwa, T., Toramaru, A., & Iguchi, M. (2009). Correlations of volcanic ash texture with explosion earthquakes from vulcanian eruptions at Sakurajima volcano, Japan. *Journal of Volcanology and Geothermal Research*, *184*(3–4), 473–486.

Nang, T. Z. W., Widiwijayanti, C., Espinosa-Ortega, T., De Groote, J., & Taisne, B. (2025). WOVOdat web service data retrieval system for comprehensive volcano monitoring. *Bulletin of Volcanology*, *87*(3), 21. https://doi.org/10.1007/s00445-025-01801-8

Newhall, C. G., Costa, F., Ratdomopurbo, A., Venezky, D. Y., Widiwijayanti, C., Win, N. T. Z., Tan, K., & Fajiculay, E. (2017). WOVOdat – An online, growing library of worldwide volcanic unrest. *Journal of Volcanology and Geothermal Research*, *345*, 184–199. https://doi.org/10.1016/j.jvolgeores.2017.08.003

Pardo, N., Cronin, S. J., Németh, K., Brenna, M., Schipper, C. I., Breard, E., White, J. D. L., Procter, J., Stewart, B., Agustín-Flores, J., Moebis, A., Zernack, A., Kereszturi, G., Lube, G., Auer, A., Neall, V., & Wallace, C. (2014). Perils in distinguishing phreatic from phreatomagmatic ash; insights into the eruption mechanisms of the 6 August 2012 Mt. Tongariro eruption, New Zealand. *Journal of Volcanology and Geothermal Research*, *286*, 397–414. https://doi.org/10.1016/j.jvolgeores.2014.05.001

Piano, L., Huanwen, P., & Bilcu, R. C. (2025). *Addressing the Depth-of-Field Constraint: A New Paradigm for High Resolution Multi-Focus Image Fusion* (arXiv:2510.19581). arXiv. https://doi.org/10.48550/arXiv.2510.19581

Puglisi, G., Reitano, D., Spampinato, L., Vogfjörd, K. S., Barsotti, S., Cacciola, L., Geyer Traver, A., Guðjónsson, D. S., Guéhenneux, Y., Komorowski, J.-C., Labazuy, P., Lemarchand, A., Nave, R., Saurel, J.-M., & Bachelery, P. (2022). The integrated multidisciplinary European volcano infrastructure: From the conception to the implementation. *Annals of Geophysics*, *65*(3), DM320. https://doi.org/10.4401/ag-8794

Spadaro, F. R., Lefèvre, R. A., & Ausset, P. (2002). Experimental rapid alteration of basaltic glass: Implications for the origins of atmospheric particulates. *Geology*, *30*(8), 671–674. https://doi.org/10.1130/0091-7613(2002)030%253C0671:ERAOBG%253E2.0.CO;2

Spampinato, L., Indovina, E., Geyer, A., Júlíusdóttir, R., Reitano, D., Puglisi, G., Nave, R., Santangelo, I., Vogfjörd, K., Labazuy, P., Cacciola, L., Domínguez-Cerdeña, I., Guehenneux, Y., Komorowski, J.-C., & Saurel, J.-M. (2024). Data and service management of the EPOS Volcano Observations Thematic Core Service by the

European volcanological community. *Bulletin of Volcanology*, *87*(1), 2. https://doi.org/10.1007/s00445-024-01780-2

Taddeucci, J., Pompilio, M., & Scarlato, P. (2002). Monitoring the explosive activity of the July–August 2001 eruption of Mt. Etna (Italy) by ash characterization. *Geophysical Research Letters*, *29*(8), 71-1-71–74. https://doi.org/10.1029/2001GL014372

Taddeucci, J., Scarlato, P., Andronico, D., Ricci, T., Civico, R., Del Bello, E., Spina, L., D'Auria, L., Asensio-Ramos, M., Calvo, D., Padrón, E., Hernández, P. A., & Pérez, N. M. (2023). The Explosive Activity of the 2021 Tajogaite Eruption (La Palma, Canary Islands, Spain). *Geochemistry, Geophysics, Geosystems*, *24*(6), e2023GC010946. https://doi.org/10.1029/2023GC010946

Tierz, P., Loughlin, S. C., & Calder, E. S. (2019). VOLCANS: An objective, structured and reproducible method for identifying sets of analogue volcanoes. *Bulletin of Volcanology*, *81*(12), 76. https://doi.org/10.1007/s00445-019-1336-3

Trasatti, E., Costa, F., & Parks, M. (2021). Editorial: The Impact of Open Science for Evaluation of Volcanic Hazards. *Frontiers in Earth Science*, *9*. https://doi.org/10.3389/feart.2021.659772

Wang, W. (2008). Rock Particle Image Segmentation and Systems. In P.-Y. Yin (Ed.), *Pattern Recognition Techniques, Technology and Applications*. InTech. https://doi.org/10.5772/6242

Widiwijayanti, C., Thin Zar Win, N., Espinosa-Ortega, T., Costa, F., & Taisne, B. (2024). The global volcano monitoring infrastructure database (GVMID). *Frontiers in Earth Science*, *12*. https://doi.org/10.3389/feart.2024.1284889

Zhao, X., Ding, W., An, Y., Du, Y., Yu, T., Li, M., Tang, M., & Wang, J. (2023). *Fast Segment Anything* (arXiv:2306.12156). arXiv. https://doi.org/10.48550/arXiv.2306.12156

Tables

Table 1: Details of samples used for ViT's evaluation and their variable coverage within the training set.

Sample details				Coverage in the training set		
Code	Volcano	Eruption date	Grain-ssize	Volcano	Sample	Microscope
KE-DB3	Kelud	14/2/14	1ϕ-2ϕ	Seen[1]	Seen	Unseen[2]
CV-DB1	Cumbre Vieja	19/10/21	0ϕ-1ϕ	Seen	Seen	Unseen
NC-DB14	Nevados de Chillán	23/1/18	0ϕ-1ϕ	Seen	Unseen	Unseen
SG-DB3	Soufrière de Guadeloupe	23/8/76	0ϕ-1ϕ	Seen	Unseen	Unseen
B-MAR	Marapi	4/12/23	1ϕ-2ϕ	Unseen	Unseen	Unseen

1: "Seen" means that particles from this volcano were used in the training set of Benet et al. (2024b) model.

2: "Unseen" means that the images were acquired with a different microscope from that of the training set images

Table 2: Results of pre-classification check across the new samples and a subset of the ViT's test set (Benet, Costa, & Widiwijayanti, 2024). Results are reported by number of particles and in percentages in brackets.

Code	# particles	Green[1]	Amber[2]	Red[3]
Test set*	100	97 (87%)	3 (3%)	0 (0%)
KE-DB3	131	26 (20%)	71 (54%)	34 (26%)
CV-DB1	62	4 (6%)	42 (68%)	16 (26%)
NC-DB14	49	5 (10%)	29 (59%)	15 (31%)
SG-DB3	99	2 (2%)	42 (42%)	55 (56%)
B-MAR	259	80 (31%)	129 (50%)	50 (19%)

* 25 randomly sampled particles for each particle type from the test set in Benet et al (2024b)

1: *Green* if it belongs to the training set distribution between 5th–97th percentiles

2: *Amber* between 97th–99th percentiles

3: *Red* beyond the 99th percentile

Table 3. Number of particles analysed, per sample componentry and accuracy per type across the five studied samples (see Table 1 for more details). For componentry, counts per particle type are shown with associated errors in parentheses, computed as the margin of error at the particle level (Benet, Costa, Widiwijayanti, et al., 2024).

Code	# particles	Componentry				F1-score				
		A[1]	F[2]	J[3]	L[4]	Macro	A	F	J	L
KE-DB3	131	62 (±11)	19 (±8)	46 (±11)	4 (±4)	0.85	0.91	0.86	0.88	0.73
CV-DB1	62	0	0	47 (±7)	15 (±7)	0.83	0.00	0.00	0.91	0.75
NC-DB14	49	6 (±4)	5 (±4)	14 (±6)	24 (±7)	0.81	0.60	0.83	0.93	0.87
SG-DB3	99	99	0	0	0	1.00	1.00	0.00	0.00	0.00
B-MAR	259	104 (±15)	48 (±12)	66 (±14)	41 (±12)	0.81	0.88	0.82	0.83	0.70
					Average:	0.86	0.85	0.84	0.89	0.76

1: A is altered material particle type

2: F is free-crystal particle type

3: J is juvenile particle type

4: L is lithic particle type